

Edge technique for direct detection of strain and temperature based on optical time domain reflectometry

Haiyun Xia,^{1,*} Chunxi Zhang,¹ Hongqian Mu,¹ and Dongsong Sun²

¹Institute of Opto-electronics Technology, Beihang University, Beijing, 100083, China

²Anhui Institute of Optics & Fine Mechanics, Chinese Academy of Sciences, Hefei, 230031, China

*Corresponding author: haiyunxia@126.com

Received 3 July 2008; revised 3 December 2008; accepted 4 December 2008;
posted 8 December 2008 (Doc. ID 98293); published 7 January 2009

A hybrid technique for real-time direct detection of strain and temperature along a single-mode fiber is proposed. The temperature is directly detected from the Raman backscattering in the time domain. To retrieve the strain profile from the Brillouin backscattering, an edge technique is introduced and a response function of the Fabry–Perot interferometer for the Brillouin backscattering is defined for the first time to our knowledge. The outgoing laser and the Brillouin backscattering are measured on different interference orders through different channels of the Fabry–Perot interferometer. A low-resolution reference channel and a high-resolution Brillouin channel are designed to keep both a high measurement sensitivity and a wide dynamic range. The measurement is based on detecting the bandwidth changes and the frequency shifts of the Brillouin backscattering; thus the resulting measurement is insensitive to the power fluctuation of the backscattering and the laser frequency jitter or drift. Neither time-consuming frequency scanning nor heavy data processing is needed, which makes real-time detection possible. The dynamic range of the edge technique can be increased substantially by using a piezoelectric tunable and capacitive-servo-stabilized Fabry–Perot interferometer. We highlight the potential of this technique by numerical simulations. Given that the uncertainty of the temperature measurement is 0.5°C and that the spatial and temporal resolutions are 10 cm and 1 s, the strain uncertainty is less than 20 $\mu\epsilon$ within a 2 km distance when the strain is below 0.4%, and it is not more than 110 $\mu\epsilon$ within a 4 km distance when the strain is below 0.6%. © 2009 Optical Society of America

OCIS codes: 060.2370, 290.1350, 290.5830, 290.5860.

1. Introduction

Fiber optic sensors have been developed for passive sensing of physical, chemical, biomedical and electrical variables. Brillouin-based sensor technology has been attractive in the past two decades for its distributed measurement, immunity to electromagnetic interference, light weight, durability, and capability to be embedded in composites. The technology can be divided into two main categories: the spontaneous Brillouin-based technique (i.e., Brillouin optical time domain reflectometry, or BOTDR) [1–7] and the

stimulated Brillouin-based technique (i.e., Brillouin optical time domain analysis) [8–13]. The dependence of the frequency shift and the intensity of the spontaneous Brillouin signal with strain and temperature have been intensively investigated to obtain the change in temperature and strain along a length of standard single-mode fiber [1–6]. Simultaneous temperature and strain measurement with a distributed Brillouin loss system was achieved [8] and was assessed by using pair-combined detection of the Brillouin frequency, power, and bandwidth, for panda, bow-tie, and tiger polarization-maintaining fibers [9–11]. The range and spatial resolution were limited mainly by the accuracy of the power measurement. To avoid the power measurement,

one elegant solution demonstrated recently was to use a multiple-composition-core sensing fiber with multiple Brillouin peaks that exhibit different frequency variations with temperature and strain. The Brillouin frequency shifts of the first two peaks were used to obtain the changes in temperature and strain simultaneously [12]. Such multippeak Brillouin backscattering was also observed in a partially Ge-doped photonic crystal fiber. Both the strain and temperature coefficients are found to be different for the two Brillouin peaks [13]. Methods for discriminating temperature and strain in spontaneous Brillouin-based distributed sensors were compared [14]. Combined detection of the spontaneous Raman and Brillouin backscattering also allows simultaneously determination of the strain and temperature [15].

To date, the candidate design of the detection system based on Brillouin backscattering usually employs coherent detection [1–15]. But it is a time-consuming process because of its frequency scanning and data processing. In dynamic conditions such as the vibrating state, the measurements may lose their reliability owing to its long detection time. For example, a system for monitoring the health of aircraft and spacecraft structures requires quick damage detection, durability, high spatial resolution, and reliability.

An alternative to coherent detection is direct detection. The conventional understanding of direct detection is that an optical interferometer, such as a Fabry–Perot interferometer (FPI), is scanned to yield the Brillouin power spectrum [5,16]. In this paper, the optical interferometer works in the static state. Our primary interest in this paper is in using the edge technique and combined detection of Raman and Brillouin components of the backscattering to achieve a real-time direct detection of both temperature and strain along a single-mode fiber without a frequency scanning process.

The edge technique is a powerful method for the detection of small frequency shifts. In particular, it has been used with lidar systems to obtain range-resolved measurements of the atmospheric wind [17,18]. With a direct-detection Doppler wind lidar, we have demonstrated that the edge technique can be used to detect the Doppler shifts (an accuracy of 1.2 MHz was achieved) [19]. In the edge technique, the frequency of the outgoing laser is located on the edge of the spectral response function of a high-resolution optical filter. Because of the steep slope of the edge, small spectrum changes of the backscattering, as a result of Doppler frequency shift and bandwidth broadening, can produce large changes in the filter transmission. So, the spectrum changes can be determined from the transmission of backscattering through the optical filter.

2. Principle of Measurement

Distributed optical fiber sensors often use Raman or Brillouin components of the scattered light in optical

fibers as the means to determine the temperature or strain. By using a pulsed laser and measuring the backscattering signal as a function of time, the backscattered light can be correlated to the distance along the fiber. In this paper, with the temperature profile detected from Raman backscattering in advance, the strain experienced along the sensing fiber can be retrieved by using a uniquely designed FPI.

A. Temperature Detection

The Raman scattered light is caused by thermally influenced molecular vibrations. It is sensitive to temperature but not to strain; consequently the backscattered light carries the information on the local temperature where the scattering occurred [20]. To accurately predict the temperature changes, the Raman signal has to be referenced to a temperature-independent signal measured with the same spatial resolution. In this paper, the temperature along the fiber is retrieved by measuring the power ratio of the Stokes to anti-Stokes Raman backscatters in the time domain. The equation relating the power ratio r_R to the temperature is given as [21]

$$r_R = p_{as}/p_s = (\lambda_s/\lambda_{as})^4 \exp(-h\Delta\nu/kT), \quad (1)$$

where p_{as} is the measured anti-Stokes power, p_s is the measured Stokes power, and λ_s and λ_{as} are the wavelengths of the Raman Stokes and the Raman anti-Stokes backscattering. Here h and k are Planck's and Boltzmann's constants, respectively. $\Delta\nu$ is the Raman shift.

B. Strain Detection

When the edge technique is used to retrieve the strain information along a sensing fiber, the Brillouin anti-Stokes backscattering provides a scattering source to detect the strain. A Brillouin channel of the interferometer is used as a frequency-to-amplitude converter to generate complementary signals, having opposite signs, and a ratio of these signals representing the Brillouin spectrum changes. With the temperature detected in advance, this ratio varies monotonically with the strain that the sensing fiber experiences. A reference channel is designed to set and measure the frequency of the outgoing laser relative to the Brillouin channel. The dynamic range of the edge technique can be increased by modulating the cavity spacing of the FPI precisely.

Brillouin scattering results from the scattering of light by sound waves. The scattered light undergoes a Doppler frequency shift ν_B , which is given by

$$\nu_B = 2n_1V_a/\lambda, \quad (2)$$

where V_a is the acoustic velocity within the fiber, n_1 is the refractive index of the fiber, and λ is the vacuum wavelength of the incident light. The strong attenuation of sound waves in silica determines the shape of the Brillouin gain spectrum. Actually, the

exponential decay of the acoustic waves results in a gain presenting a Lorentzian spectral profile [22]:

$$g_B(\nu) = g_0[1 + (\nu - \nu_B)^2 / (w_B/2)^2]^{-1}, \quad (3)$$

where w_B is the full width at half-maximum (FWHM). The Brillouin gain spectrum peaks at the Brillouin frequency shift ν_B , and the peak value is given by the Brillouin gain coefficient

$$g_0 = 2\pi n_1^7 p_{12}^2 / c \lambda_p^2 \rho_0 V_a w_B, \quad (4)$$

where p_{12} is the longitudinal elastic-optic coefficient, ρ_0 is the density, λ_p is the pump wavelength, and c is the vacuum velocity of light. Within a limited dynamic range, ν_B and w_B are expressed as a linear function of strain ε and temperature T as

$$\nu_B(T, \varepsilon) = \nu_B(T_0, 0) + c_{\nu_B}^{\varepsilon} \varepsilon + c_{\nu_B}^T (T - T_0), \quad (5)$$

$$w_B(T, \varepsilon) = w_B(T_0, 0) + c_{w_B}^{\varepsilon} \varepsilon + c_{w_B}^T (T - T_0). \quad (6)$$

In the above two equations, T_0 is the reference temperature (25°C), $c_{\nu_B}^{\varepsilon}$, $c_{\nu_B}^T$, and $c_{w_B}^{\varepsilon}$, $c_{w_B}^T$ are the temperature and strain coefficients for the Brillouin shift and spectrum broadening, respectively. Here $\nu_B(T_0, 0)$ and $w_B(T_0, 0)$ are the Brillouin shift and the FWHM of the spectrum when the sensing fiber is free of strain and at the reference temperature.

Because the spatial resolution is determined by the launched pulse width, a short light pulse is required to improve the spatial resolution. However, as the pulse width becomes shorter, the bandwidth of the Brillouin backscattered light broadens rapidly, and the power spectrum may change from its original Lorentzian shape when the pulse width falls below approximately 30 ns [23–25]. The power spectrum of the Brillouin backscattering is the convolution of the pulse spectrum $S_P(\nu)$ and the Brillouin gain spectrum:

$$S_B(\nu, T_D, \varepsilon) = S_0(\nu, T_D, \varepsilon) \otimes S_P(\nu), \quad (7)$$

where the peak normalized Brillouin spectrum $S_0(\nu, T_D, \varepsilon)$ corresponding to temperature T_D and tensile strain ε is given by

$$S_0(\nu, T_D, \varepsilon) = \{1 + [\nu - \nu_B(T_D, \varepsilon)]^2 / [w_B(T_D, \varepsilon)/2]^2\}^{-1}. \quad (8)$$

As shown in Eq. (5) and (6), both the Doppler shift and spectrum bandwidth of the Brillouin backscattering are sensitive to temperature and strain. However, with the temperature detected in advance, the edge technique can be implemented to retrieve the strain the sensing fiber experienced. Two major changes are made to the original edge technique [19]. First, a low-resolution reference channel and a high-

resolution Brillouin channel are designed to keep both a high measurement sensitivity and a large dynamic range. Second, the frequency of the outgoing laser and the frequency of the Brillouin backscattering are measured on different interference orders through different channels of the FPI.

In considering an ideal FPI we assume that the plates that make up the FPI are perfectly flat and ideally parallel to each other. The FPI consists of two channels with different cavity spacings and different plate reflectivities that form the transmission curves as shown in Fig. 1. The interferometer is illuminated by a fiber collimated on the two channels (semicircle shape) with an angular field of view of θ_{\max} (semi-angle). Therefore, the edge function is the result of the integration of the Airy function over the angle of incidence θ , which can be expressed as

$$h(\nu) = \int_0^{\theta_{\max}} T_p / \{1 + 4(\nu_{\text{FSR}} / \pi \nu)^2\} \times \sin^2[\pi \nu \cos(\theta) / \nu_{\text{FSR}}] d\theta, \quad (9)$$

where T_p is the peak transmission and ν_F is the FWHM of the FPI; ν_{FSR} is the free-spectral range (FSR) of the FPI, which is given by

$$\nu_{\text{FSR}} = c / 2n_2l, \quad (10)$$

where l is the cavity spacing and n_2 is the reflective index of the FPI. As is shown in Fig. 1, the wider curve denoted the reference channel (h_R) is used to preset and to detect the frequency of the outgoing laser relative to the FPI, and the narrower curve denoted the Brillouin channel (h_B) is used to detect the spectrum changes of the Brillouin backscattering.

Since a single-cavity-spacing structure is used in the FPI, the two transmission curves have nearly the same frequency period of FSR [19]. As is shown in Fig. 1, the frequency separation between the two curves is designed to be $\nu_{\text{BR}} = 200$ MHz. So, when the frequency of the outgoing laser pulse is detected

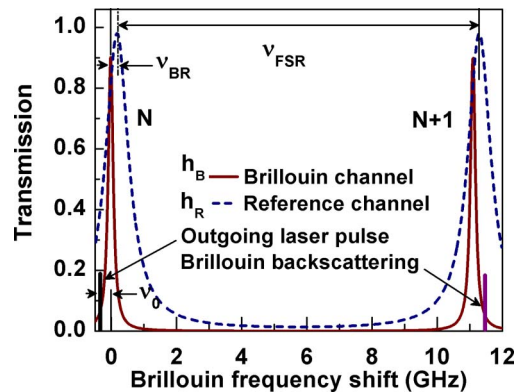


Fig. 1. (Color online) Spectral profiles of the twin-channel FPI. The frequency centers of the outgoing laser pulse and the Brillouin backscattering are labeled. Interference orders of the FPI are marked.

relative to the FPI, the laser pulse is located on the sharp wing of the reference channel. Using transmission values of the reference channel for the outgoing laser as the feedback to modulate the piezoelectric drivers of the FPI, one can preset the frequency offset of the outgoing laser pulse relative to the peak of the Brillouin channel (i.e., ν_0 on the interference order of N). The Brillouin anti-Stokes backscattering is analyzed through the Brillouin channel of the interference order of $N + 1$. So, the Brillouin backscattering spectrum should be located on the steep wing of the Brillouin channel of the order of $N + 1$ to yield a high sensitivity.

The operating principle of the FPI as an analyzer is shown in Fig. 2. Before retrieving the strain profile along the sensing fiber, the temperature profile is detected. The Brillouin frequency shift $\nu_B(T_{\min}, 0)$ corresponding to the minimum temperature T_{\min} and null strain can be calculated from Eq. (5). The frequency of the Brillouin backscattering spectrum $S_B(\nu, T_{\min}, 0)$ relative to the peak of the Brillouin channel of the interference order of $N + 1$ can be set to a definite value of $\nu_1 = 100$ MHz. Then the frequency offset ν_0 to be preset is given by

$$\nu_0 = \nu_{\text{FSR}} + \nu_1 - \nu_B(T_{\min}, 0). \quad (11)$$

By shrinking or stretching the piezoelectric stacks of a small fraction of a FSR, one can preset the Brillouin backscattering spectrum $S_B(\nu, T_{\min}, \epsilon)$ on the steep wing of Brillouin channel of interference order $N + 1$. The cavity spacing change Δl is given by

$$\Delta l = -\nu_0 \lambda / c. \quad (12)$$

For example, given $T_{\min} = T_0$, $l = 13.5$ mm, $\lambda = 1553$ nm, and $\nu_{\text{FSR}} = \nu_B(T_0, 0)$, the frequency offset ν_0 should be set to 100 MHz according to Eq. (11); thus the FPI plates should come closer to 6.99 nm according to Eq. (12).

A piezoelectric-tunable and capacitive-servo-stabilized FPI is proposed to achieve the aforementioned initialization (IC Model ET50FS-1049 was used in [19]). A capacitance bridge fabricated on the mirror plates is used to sense changes in paral-

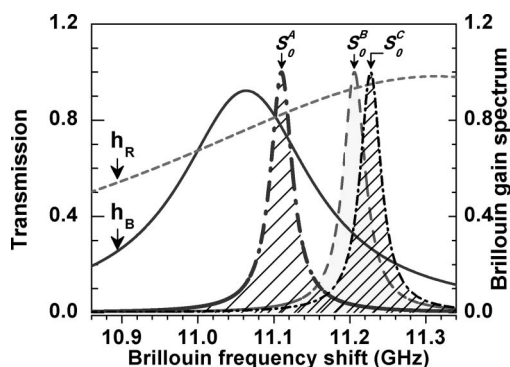


Fig. 2. The FPI transmissions of the interference order of $N + 1$ and the Brillouin gain spectrums. S_0^A , S_0^B , and S_0^C corresponding to $(25^\circ\text{C}, 0\epsilon)$, $(25^\circ\text{C}, 2m\epsilon)$ and $(45^\circ\text{C}, 2m\epsilon)$, respectively.

lelism and cavity spacing of the FPI. Electronic closed-loop control can stabilize the capacitance gap to better than 0.1 nm rms. Three piezoelectric actuators are used to turn the cavity spacing and permit elimination of parallelism errors.

At a detected temperature T_D , the transmission of the Brillouin channel for the Brillouin backscattering varies with the strain the fiber experienced, which is given by

$$\tau(\epsilon)_{T_D} = \int_{-\infty}^{\infty} S_B(\nu, T_D, \epsilon) h_B(\nu + \nu_0) d\nu / \int_{-\infty}^{\infty} S_B(\nu, T_D, \epsilon) d\nu. \quad (13)$$

$\tau(\epsilon)_{T_D}$ can be measured conveniently. Then, nonlinear equation (13) can be solved for the strain information. However, to make full use of the Brillouin backscattering, we define a strain response function at temperature T_D as

$$R(\epsilon)_{T_D} = \tau(\epsilon)_{T_D} / [1 - \tau(\epsilon)_{T_D}]. \quad (14)$$

The physical meaning of Eq. (14) is explicit. It is the ratio of the transmission and the reflection of the Brillouin channel for the Brillouin backscattering. With the detected ratio $R(\epsilon)_{T_D}$, Eq. (14) can be solved for strain. The detection of the ratio $R(\epsilon)_{T_D}$ is introduced in Section 2.C in detail.

Figure 3 shows the response curves versus the strain at different temperatures. One problem is that the response curve becomes gentle when temperature increases, which will lead to a low measurement sensitivity. This is because the Brillouin backscattering can even run out the reach of the Brillouin channel when the sensing fiber goes through some harsh environment. Fortunately, the backscattering is range gated in the BOTDR system. If the sensing fiber undergoes a wide temperature range along the fiber, one can retrieve the strain profile by setting a different frequency offset ν_0 in each subsection according to the temperature range. Thus, the dynamic range of measurement can be extended substantially.

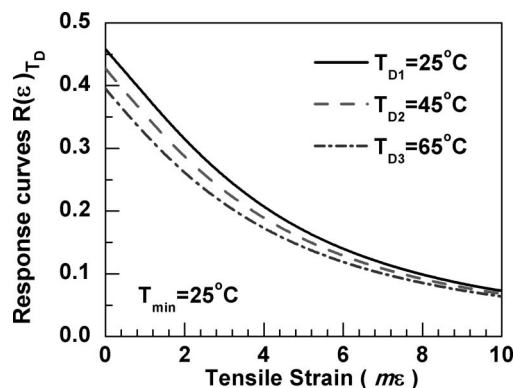


Fig. 3. Response function versus the tensile strain the fiber experienced at different temperature when the minimum temperature is 25°C .

C. System Description

The schematic diagram of the proposed system is shown in Fig. 4. It was found that Raman scattering has a lower gain coefficient, causing the Raman scattered power to be about 10 dB less than that of Brillouin scattering. To measure the temperature profile based on Raman scattering along the sensing fiber, there is a need to generate a high peak power within a short pulse. So the light generated from a continuous-wave distributed-feedback laser diode is amplified by an Er-doped fiber amplifier (EDFA1). A LiNbO₃ electro-optic modulator (EOM) externally modulates the output power to generate laser pulses. Before launching into the sensing fiber (SF), a small fraction of the output power is split out as the reference signal by the fused fiber coupler (C1) for measuring the frequency of the outgoing pulse relative to the FPI. The reference signal passing through the circulator (CIR1) is collimated by a fiber collimator (CLM1) onto the reference channel of the FPI. The transmitted light is coupled into a photodetector (DET1) by using a fiber coupler (CPL1). The reflected light from the reference channel is coupled by CLM1 and guided into DET2 through CIR1 and fiber coupler C2. With the power ratio of the outputs from DET1 and DET2 and the transmission function $h_R(\nu)$ calibrated in advance, one can determine ν_0 (i.e., the frequency of the laser pulse relative to the FPI of interference order N).

The major portion of the laser pulse is launched into the sensor fiber (SF) via a polarization scrambler (PS) and a reference coil (RC). The residual amplified spontaneous emission noise is filtered by an in-fiber Bragg grating (BG1) in conjunction with a circulator. The Rayleigh backscattering is about 30 dB stronger than the Raman anti-Stokes backscattering. It is estimated that the Rayleigh signal must be suppressed by at least 33 dB to reduce the effects of coherent Rayleigh noise to an acceptable level in a BOTDR system [2]. Hence, the backscattering exiting the CIR2 is filtered by BG2 and BG3 used in cascade with an isolator (ISO2) to prevent the formation of an etalon. In this way, the combined filter offers minimum attenuation to the Brillouin and the Raman

components. A wavelength division multiplexer (WDM) is used to single out the Brillouin and the Raman signals. It also provides further rejection of the Rayleigh signal. With the ratio of output powers from DET3 and DET4, the temperature along the sensing fiber can be determined according to Eq. (1). The Brillouin backscattering exiting the WDM propagates into the Brillouin channel through BG4, EDFA2, CIR3, and CLM2. Only Brillouin anti-Stokes backscattering is used for the sensing, so BG4 centered at the Brillouin Stokes frequency is used to reject the Brillouin Stokes backscattering. The anti-Stokes Brillouin backscattering is amplified by EDFA2. The residual amplified spontaneous emission noise was filtered by BG5 in conjunction with CIR3. The transmitted and reflected signals are measured on DET1 and DET2, respectively.

With consideration of the reliability and thermostability of the system, all circulators, fused fiber couplers, fiber Bragg gratings, and the FPI are cased in an attenuator and maintained at a temperature of $25^\circ\text{C} \pm 0.1^\circ\text{C}$. Other features of the system can include a reference fiber coil (RC) experiencing null strain in the attenuator, which allows all other measurements to be calibrated.

3. Analysis

In the proposed apparatus, the major components affecting the measurement accuracy are the FPI and the EOM. The design of the dual-channel FPI and the operation of the EOM are discussed in this section.

A. Optimization of the FPI

As shown in Fig. 2, the gentler the slope of the Brillouin channel, the less sensitive but wider the dynamic range. To keep both high sensitivity and wide dynamic range, a twin-channel FPI is used. The narrow channel is optimized for analyzing the Brillouin backscatter, and the broad channel is used to preset and measure the frequency offset ν_0 .

The optimization process of the Brillouin channel is similar to that for the edge technique used in Doppler lidar systems. The value of ν_{FSR} is designed to be $\nu_B(T_0, 0)$. There is a step between the two semi-circles on one piece of the FPI plates, which produced a 200 MHz frequency separation between the transmission peaks of the Brillouin channel and the reference channel. The FWHM of the Brillouin channel ν_{FB} is designed to be $0.6w_B(T_0, 0)$. The factor 0.6 is an empirical factor in the edge technique [18]. The FWHM of the reference channel ν_{FR} is designed to be 1 GHz according to the measurement dynamic range.

Generally, the FPI is not illuminated with a perfectly collimated incident light. In practice, a small beam divergence of the incident signal is allowed at the sacrifice of degrading the passband characteristic of the FPI. To preserve the high-resolution property of the FPI, a maximum semi-divergence-angle θ_M is defined as [26]

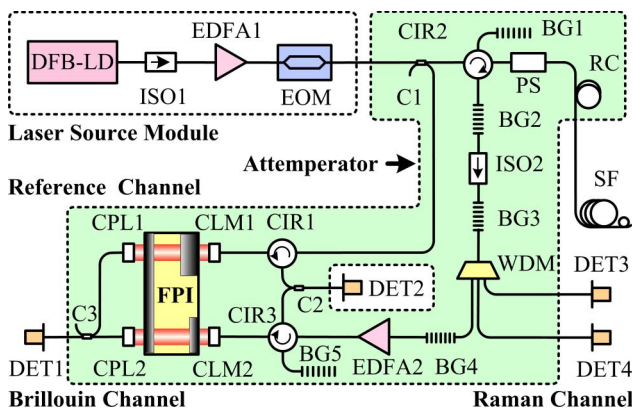


Fig. 4. (Color online) Schematic diagram of the proposed apparatus.

$$\theta_M = (2\nu_F/\nu)^{1/2}. \quad (15)$$

To discuss the working aperture (D_{FPI}) requirement of the individual channel, we consider the FPI etendue, i.e., the area solid-angle product, which is given by

$$(A\Omega)_{\text{FPI}} = \frac{1}{2}(\pi D_{\text{FPI}})^2 \int_0^{\theta_M} \sin(\theta) d\theta. \quad (16)$$

By conservation of optical throughput, the FPI must match or exceed the etendue defined by the optical components preceding it. For this system, the initial system etendue depends on the core diameter (D_f) and the numerical aperture (NA) of the sensing fiber, which is given by

$$(A\Omega)_F = \frac{1}{2}(\pi D_f)^2 \int_0^{\sin(\text{NA})} \sin(\theta) d\theta. \quad (17)$$

Thanks to the tiny core diameter of the single-mode fiber, the FPI aperture required is usually small than 1 mm. Fiber optic collimators are commercially available (Newport, F-H10). High-precision optics delivers a semidivergence of 0.25 mrad and a beam diameter of 5 mm at the working wavelength of 1553 nm. In contrast, the diameter of the FPI can be manufactured to be as large as 132 mm [27]; thus hundreds of channels can be fabricated onto a single FPI system.

Furthermore, if the beam divergence of the signal illuminating the FPI is far below the maximum divergence defined by Eq. (15), then Eq. (9) can be expressed as a Lorentzian function

$$h'(\nu) = T_p [1 + \nu^2/(\nu_F/2)^2]^{-1}. \quad (18)$$

This expression will further simplify the data processing.

B. Operation of the EOM

When a pulsed light is launched into an optical fiber to measure strain or temperature by analysis of the Brillouin backscattering, the pulse width must be short to improve the spatial resolution. However, it has been reported that, as the pulse width becomes shorter, the bandwidth of the Brillouin backscattered light becomes wider and the power spectrum changes from its original Lorentzian shape. The relation between the pulse modulation and the resultant power spectrum of spontaneous Brillouin backscattering was analyzed theoretically and discussed experimentally [23–25].

The electric field of the launched pulsed light depends on the modulating signal fed to the EOM. To simplify the data processing, thus to guarantee a fast detection of strain along the sensing fiber, an exponential-decay signal $E(t) = \exp(-t/2W)$ is proposed to modulate the EOM, where W is the pulse width in the time domain. The pulse has a constant optical frequency ν_L in the frequency domain within

the pulse duration. Then, the peak-normalized power spectrum of the pulse is given by

$$S_P(\nu) = \{1 + [2\pi W(\nu - \nu_L)]^2\}^{-1}. \quad (19)$$

By substituting Eq. (7), (18), and (19) into Eq. (13), one can find that the transmission of the Brillouin channel for the Brillouin backscattering can also be expressed as a Lorentzian function rather than a Voigt function. This will substantially simplify the data processing.

4. Simulations

To evaluate the performance, we present the results of numerical simulations of the above system. Temperature and strain coefficients of the Brillouin bandwidth in different polarization-maintaining fibers were studied with the stimulated Brillouin-based technique [8]. However, previous work seldom focused on the bandwidth characteristic of the Brillouin backscattering. The bandwidth characteristic of the Brillouin backscattering from a single-mode fiber has not been studied at 1.55 μm as far as we know.

The Brillouin bandwidth (FWHM) is given by [28]

$$w_B = \Gamma'(4n_1\pi/\lambda)^2, \quad (20)$$

where Γ' is a damping parameter that can be shown as

$$\Gamma' = \frac{1}{\rho_0} \left[\frac{4}{3}\eta_S + \eta_b + \frac{\kappa}{c_p}(\gamma - 1) \right], \quad (21)$$

where η_S is the shear viscosity coefficient, η_b is the bulk viscosity coefficient, κ is the thermal conductivity, c_p is the specific heat at constant pressure, and γ is the adiabatic index. From Eqs. (20) and (21), one can see that Γ' is determined by the optical material of the sensing fiber. So the Brillouin bandwidth coefficients at wavelength of 1.553 μm can be deduced from the previous work done at 1.32 μm [29]. All simulation parameters are listed in Table 1.

When an optical pulse of peak power ($p_0 = 2\text{ W}$) and pulse width ($W = 1\text{ ns}$) is injected into an optical fiber, the Brillouin backscattering power p_B observed at the input fiber end is given as [16]

$$p_B = (Gp_0S\alpha_B Wv/2) \exp(-2az), \quad (22)$$

where G is the gain of EDFA2, S is the backscatter recapture fraction given by $(\lambda/\pi n_1 \omega)^2/4$, where $\omega = 4.5\text{ }\mu\text{m}$ is the mode field radius of the fiber, α_B is the Brillouin backscattering coefficient given by $7.1 \times 10^{-30}/\lambda^4$ at room temperature, $\alpha = 0.2\text{ dB/km}$ is the fiber loss, z is the propagating pulse's location in the fiber, and v is the light's velocity in the fiber.

When InGaAs avalanche photodiodes capable of single-photon detection are used, the photon rate corresponding to Brillouin backscattering power detected on DET1 is given by

Table 1. Parameters of the Proposed System

Variable	Value	Units	Ref.
$\nu_B(T_0, 0)$	11.11	GHz	[13]
$w_B(T_0, \epsilon)$	35	MHz	[13]
$c_{\nu_B}^{\epsilon}$	0.048	MHz/ $\mu\epsilon$	[13]
$c_{\nu_B}^T$	1.07	MHz/ $^{\circ}\text{C}$	[13]
$c_{w_B}^{\epsilon}$	0	MHz/ $\mu\epsilon$	[29]
$c_{w_B}^T$	-0.095	MHz/ $^{\circ}\text{C}$	[29]
G	40	dB	[30]
NEP	3×10^{-16}	W/Hz $^{1/2}$	[31]

$$N_1 = \eta_1 \eta_2 p_B \tau(\epsilon)_{T_D} / (hc/\lambda), \quad (23)$$

where $\eta_1 = 0.6$ is the detector quantum efficiency and η_2 is the product of the optical efficiencies of all optical elements before DET1. Similarly, the photon rate detected with DET2 is given by

$$N_2 = \eta_1 \eta_3 p_B [1 - \tau(\epsilon)_{T_D}] / (hc/\lambda), \quad (24)$$

where η_3 is the product of the optical efficiencies of all optical elements before DET2. With the ratio of outputs from DET1 and DET2, $R(\epsilon)_{T_D}$ in Eq. (14) can be determined; thus the strain profile along the sensing fiber can be retrieved.

According to Eq. (14), one can find that in this direct-detection method the strain profile is retrieved by analyzing the transmission changes of Brillouin backscattering throughout the FPI. The uncertainty in the strain measurement is given by

$$\delta_1(\epsilon) = \delta[R(\epsilon)_{T_D}] / \Theta(\epsilon), \quad (25)$$

where $\Theta(\epsilon)$ is defined as the measurement sensitivity given by $d[R(\epsilon)_{T_D}] / d\epsilon$. In this work, η_2 and η_3 are evaluated to be 0.75, so, from Eqs. (23) and (24), Eq. (14) becomes $R(\epsilon)_{T_D} = N_1 / N_2$. In photon timing the noise in the measurement of the optical waveform is given by the Poissonian fluctuations of the number of events (caused by both signal photons and dark counts) that are collected within the bin width ($\Delta_t = 1$ ns). Therefore, given the photon counting rates N_1 and N_2 , for 1 s of integration time, the uncertainty in the measurement of $R(\epsilon)_{T_D}$ is given by

$$\delta^2[R(\epsilon)_{T_D}] = \left\{ \frac{[(N_1 + N_D)R\Delta_t]^{1/2}}{N_2 R \Delta_t} \right\}^2 + \left\{ \frac{N_1 [(N_2 + N_D)R\Delta_t]^{1/2}}{N_2^2 R \Delta_t} \right\}^2, \quad (26)$$

where N_D is the dark-counting rate given by $0.5(\eta_1 \text{NEP} / h\nu_L)^2$, where NEP is the noise equivalent power of the single-photon counting detector and $R = 1 \times 10^4$ Hz is the pulse repetition rate employed in the measurement.

Strain measurement uncertainties versus tensile strain and the pulse propagating location at different temperature are shown in Fig. 5 on a logarithmic scale. The temporal resolution is 1 s and the spatial

resolution is 10 cm. It can be seen from the contour lines that the strain uncertainty is below $10 \mu\epsilon$ within a 2 km distance when the tensile strain is below 0.4%, and not more than $100 \mu\epsilon$ within a 4 km distance when the tensile strain is below 0.6%. Given a fixed distance, the minimum uncertainty occurs in the vicinity of 0.2% because the measurement sensitivity $\Theta(\epsilon)$ peaks there. The strain measurement accuracy will decrease when the strain becomes large; this is because the Brillouin backscattering spectrum reaches the piedmont part of the Brillouin channel, as shown in Fig. 2.

The Brillouin spectrum is sensitive to changes in both temperature and strain. So, in the strain retrieving process, the strain detection also depends on the accuracy of the temperature detected. If the uncertainty in the temperature and strain coefficients for both Brillouin frequency and bandwidth are ignored, accounting for only the uncertainty induced by the uncertainty of temperature measurements, one can determine the uncertainty for the strain measurements as

$$\delta_2(\epsilon) = |[\partial R(\epsilon)_{T_D} / \partial T] \delta(T)| / \Theta(\epsilon), \quad (27)$$

where $\delta(T)$ is the uncertainty of the temperature detection. Figure 6 shows the dependence of strain measurements on the uncertainty of the temperature detections. It is obvious that to achieve a strain resolution better than $10 \mu\epsilon$, the uncertainty of temperature measurements should not be higher than 0.5°C .

5. Conclusion

An edge technique was introduced to retrieve the tensile strain profile along a single-mode fiber. The temperature profiles along the sensing fiber are directly detected by measuring the power ratio of the Stokes to anti-Stokes Raman backscatters in the time domain. With the detected temperature, the strain experienced on the sensing fiber can be

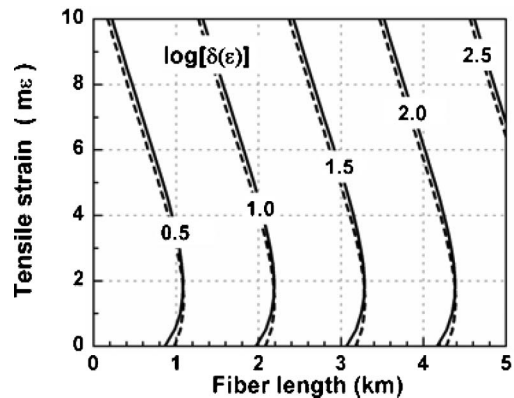


Fig. 5. Strain measurement uncertainty versus tensile strain and length of the sensing fiber. The solid and dashed contour lines correspond to detected temperatures of 25°C and 45°C , respectively. The minimum temperature is 25°C .

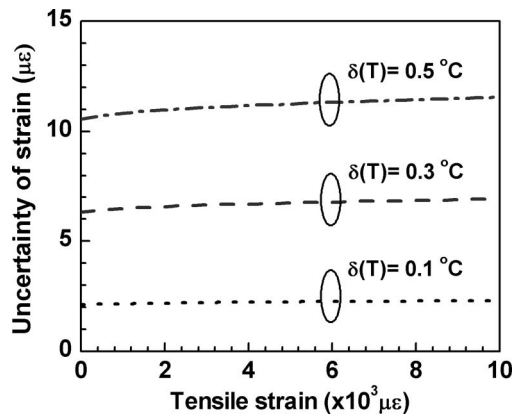


Fig. 6. Dependence of strain measurements on the uncertainty of temperature measurements. Both the minimum temperature and the detected temperature are 25°C.

retrieved by analyzing the Brillouin backscattering by using a Fabry-Perot interferometer (FPI).

This method can avoid time-consuming frequency scanning and the heavy processing load of deducing a peak or average frequency from the Brillouin spectrum. The dynamic range of the measurement can be extended by presetting the frequency offset of the outgoing laser relative to the FPI. Although the FPI systems are usually expensive, hundreds of BOTDR sensing fibers can be integrated onto a single FPI. A mathematical mode is built to evaluate the performance of the system proposed in this work. Simulations show that this pure direct-detection method is suitable for strain and temperature detection in dynamic conditions with high spatial resolution of 10 cm.

References

1. T. Kurashima, T. Horiguchi, and M. Tateda, "Thermal effects of Brillouin gain spectra in single-mode fibers," *IEEE Photon. Technol. Lett.* **2**, 718–720 (1990).
2. P. C. Wait and A. H. Hartog, "Spontaneous Brillouin-based distributed temperature sensor utilizing a fiber Bragg grating notch filter for the separation of the Brillouin signal," *IEEE Photon. Technol. Lett.* **13**, 508–510 (2001).
3. H. H. Kee, G. P. Lees, and T. P. Newson, "All-fiber system for simultaneous interrogation of distributed strain and temperature sensing by spontaneous Brillouin scattering," *Opt. Lett.* **25**, 695–697 (2000).
4. T. R. Parker, M. Farhadiroushan, V. A. Handerek, and A. J. Rogers, "Temperature and strain dependence of the power level and frequency of spontaneous Brillouin scattering in optical fibers," *Opt. Lett.* **22**, 787–789 (1997).
5. T. R. Parker, M. Farhadiroushan, V. A. Handerek, and A. J. Rogers, "A fully distributed simultaneous strain and temperature sensor using spontaneous Brillouin backscatter," *IEEE Photon. Technol. Lett.* **9**, 979–981 (1997).
6. T. R. Parker, M. Farhadiroushan, R. Feced, V. A. Handerek, and A. J. Rogers, "Simultaneous distributed measurement of strain and temperature from noise-initiated Brillouin scattering in optical fibers," *IEEE J. Quantum Electron.* **34**, 645–659 (1998).
7. J. Geng, S. Staines, M. Blake, and S. Jiang, "Distributed fiber temperature and strain sensor using coherent radio-frequency detection of spontaneous Brillouin scattering," *Appl. Opt.* **46**, 5928–5932 (2007).

8. X. Bao, D. J. Webb, and D. A. Jackson, "Combined distributed temperature and strain sensor based on Brillouin loss in an optical fiber," *Opt. Lett.* **19**, 141–143 (1994).
9. X. Bao, Q. Yu, and L. Chen, "Simultaneous strain and temperature measurements with polarization-maintaining fibers and their error analysis by use of a distributed Brillouin loss system," *Opt. Lett.* **29**, 1342–1344 (2004).
10. Q. Yu, X. Bao, and L. Chen, "Temperature dependence of Brillouin frequency, power, and bandwidth in panda, bow-tie, and tiger polarization-maintaining fibers," *Opt. Lett.* **29**, 17–19 (2004).
11. Q. Yu, X. Bao, and L. Chen, "Strain dependence of Brillouin frequency, intensity, and bandwidth in polarization-maintaining fibers," *Opt. Lett.* **29**, 1605–1607 (2004).
12. C. C. Lee, P. W. Chiang, and S. Shi, "Utilization of a dispersion-shifted fiber for simultaneous measurement of distributed strain and temperature through Brillouin frequency shift," *IEEE Photon. Technol. Lett.* **13**, 1094–1096 (2001).
13. L. Zou, X. Bao, A. V. Shahraam, and L. Chen, "Dependence of the Brillouin frequency shift on strain and temperature in a photonic crystal fiber," *Opt. Lett.* **29**, 1485–1487 (2004).
14. M. N. Alahbabi, Y. T. Cho, and T. P. Newson, "Comparison of the methods for discriminating temperature and strain in spontaneous Brillouin-based distributed sensors," *Opt. Lett.* **29**, 26–28 (2004).
15. M. N. Alahbabi, Y. T. Cho, and T. P. Newson, "Simultaneous temperature and strain measurement with combined spontaneous Raman and Brillouin scattering," *Opt. Lett.* **30**, 1276–1278 (2005).
16. T. Horiguchi, K. Shimizu, T. Kurashima, M. Tateda, and Y. Koyamada, "Development of a distributed sensing technique using Brillouin scattering," *J. Lightwave Technol.* **13**, 1296–1302 (1995).
17. C. L. Korb, B. M. Gentry, and S. X. Li, "Edge technique Doppler lidar wind measurements with high vertical resolution," *Appl. Opt.* **36**, 5976–5983 (1997).
18. J. A. McKay, "Modeling of direct detection Doppler wind lidar. I. the edge technique," *Appl. Opt.* **37**, 6480–6486 (1998).
19. H. Xia, D. Sun, Y. Yang, F. Shen, J. Dong, and T. Kobayashi, "Fabry-Perot interferometer based Mie Doppler lidar for low tropospheric wind observation," *Appl. Opt.* **46**, 7120–7131 (2007).
20. P. C. Wait, S. Gaubicher, J. M. Sommer, and T. P. Newson, "Raman backscatter distributed temperature sensor based on a self-starting passively mode locked fiber ring laser," *Electron. Lett.* **32**, 388–389 (1996).
21. R. M. Measures, *Structural Monitoring with Fiber Optic Technology* (Academic, 2001).
22. D. Heiman, D. S. Hamilton, and R. W. Hellwarth, "Brillouin scattering measurements on optical glasses," *Phys. Rev. B* **19**, 6583–6589 (1979).
23. H. Naruse and M. Tateda, "Trade-off between the spatial and the frequency resolutions in measuring the power spectrum of the Brillouin backscattered light in an optical fiber," *Appl. Opt.* **38**, 6516–6521 (1999).
24. H. Naruse and M. Tateda, "Launched pulse-shape dependence of the power spectrum of the spontaneous Brillouin backscattered light in an optical fiber," *Appl. Opt.* **39**, 6376–6384 (2000).
25. J. Smith, A. Brown, M. DeMerchant, and X. Bao, "Pulsewidth dependence of the Brillouin loss spectrum," *Opt. Commun.* **168**, 393–398 (1999).
26. P. Jacquinot, "The luminosity of spectrometers with prisms, gratings, or Fabry-Perot etalon," *J. Opt. Soc. Am.* **44**, 761–765 (1954).
27. J. A. McKay and D. Rees, "High-performance Fabry-Perot etalon mount for spaceflight," *Opt. Eng.* **39**, 315–319 (2000).

28. Robert W. Boyd, *Nonlinear Optics*, 2nd ed. (Academic, 2003).
29. M. Nikles, L. Thevenaz, and P. A. Robert, "Brillouin gain spectrum characterization in single-mode optical fibers," *J. Lightwave Technol.* **15**, 1842–1851 (1997).
30. Y. Li, F. Zhang, and T. Yoshino, "Wide-range temperature dependence of Brillouin shift in a dispersion-shifted fiber and its annealing effect," *J. Lightwave Technol.* **21**, 1663–1667 (2003).
31. A. Lacaíta, F. Zappa, S. Cova, and P. Lovati, "Single-photon detection beyond $1\ \mu\text{m}$: performance of commercially available InGaAs/InP detectors," *Appl. Opt.* **35**, 2986–2996 (1996).